Supporting Information

Near-Field Thermophotovoltaic Conversion with High Electrical Power Density and Cell Efficiency above 14%

Christophe Lucchesi,[†] Dilek Cakiroglu,[‡] Jean-Philippe Perez,[‡] Thierry Taliercio,[‡] Eric Tournié,[‡] Pierre-Olivier Chapuis,[†] Rodolphe Vaillon, [‡,†,*]

[†]Univ Lyon, CNRS, INSA-Lyon, Université Claude Bernard Lyon 1, CETHIL UMR5008, F-69621, Villeurbanne, France

[‡]IES, Univ Montpellier, CNRS, Montpellier, France

Outline

1. Main experimental methods

Fabrication of the emitter

The emitter (Fig. 1b) consists of a commercial doped-Si scanning thermal microscopy probe (VITA-HE-NANOTA-200 from Bruker) on which a graphite sphere was glued using a 600 nm particle size Al_2O_3-based ceramic adhesive (RESBOND 989F) which can withstand temperatures up to 1920 K. The sphere of diameter 37.5 µm (Carbon powder from Goodfellow) was heated by the doped-Si tip of the SThM probe. Graphite was selected from an analysis of various materials (Supplementary Fig. 3a,b). The electrical resistance of the probe and its dependence on temperature allowed simultaneous temperature measurements and heating by Joule effect of the sphere up to approximately 1200 K. Above this temperature and until the melting temperature of silicon (1687 K), the electrical resistance variations are insufficient to perform accurate temperature measurements, but the emitter can still be heated (Supplementary Fig. 1a).

Calibration curve of the emitter temperature

Each emitter had to be calibrated in temperature by measuring the electrical resistance dependence on temperature of the scanning thermal microscopy probe to which it was glued [2]. First, the whole system composed of the SThM probe and its half-moon shaped holder was put in an oven typically used for thermocouples calibration (Fluke 9144). Because of the holder, the electrical resistance measurement could only be performed from room temperature to 413 K (140 °C). At higher temperatures, the glue and other components of the holder started to deteriorate and the probe could be damaged. To retrieve the $R(T)$ curve at these higher temperatures, a measurement of the resistance according to electrical power was performed. A current source provided an electrical current to the probe up to 11 mA while the probe voltage was measured so the resistance could be calculated. This kind of doped-Si probe has a characteristic $R(T)$ curve with a maximum resistance $R_{\max}$ for a given temperature $T_{R\max}$ which depends on the doping level of the low-doped part of the probe, located near the tip (Supplementary Fig. 1). At this point, the thermally generated carrier concentration becomes higher than the doping level and the temperature evolution becomes linear with electrical power[1]. For the resistance measurement at $T < T_{R\max}$ made in the oven, the data could be well fitted with a quadratic model up to a few kelvins before $T_{R\max}$. For $T > T_{R\max}$ the temperature rise was calculated here from the electrical power by multiplying with a fitting factor so both temperature scales matched near $T_{R\max}$. Put together, the data from the direct measurement in the oven and the $R(P)$ electrical measurement gave the $R(T)$ curve for the entire temperature range (see Supplementary Fig. 1). Note that the whole procedure considers that the temperature measured by the electrical resistance and the apex temperature are identical, which is an approximation. Our relative error on temperature was determined by an independent optical measurement of the temperature close to the apex. For the peak temperature, it was found to be around 5%. The main error is above 850 K, where the uncertainty becomes larger.

The temperature coefficient of the electrical resistivity (TCR) $\alpha = \frac{1}{R}\frac{dR}{dT}$ allows determining the temperature T_S for which the sensitivity is maximum. The determination of the TCR is very sensitive to the applied procedure. For the considered SThM probes and for the abovementioned procedure, T_S is around 732 K and corresponds to the maximum value (in absolute values) of α, where a small change in temperature induces a large change in electrical resistance that can be measured more easily. Beyond around 1200 K, the sensitivity becomes very low and it is therefore complicated to accurately determine the temperature based on the resistance measurement. More information can be found in the Ph.D. thesis by Lucchesi[2].

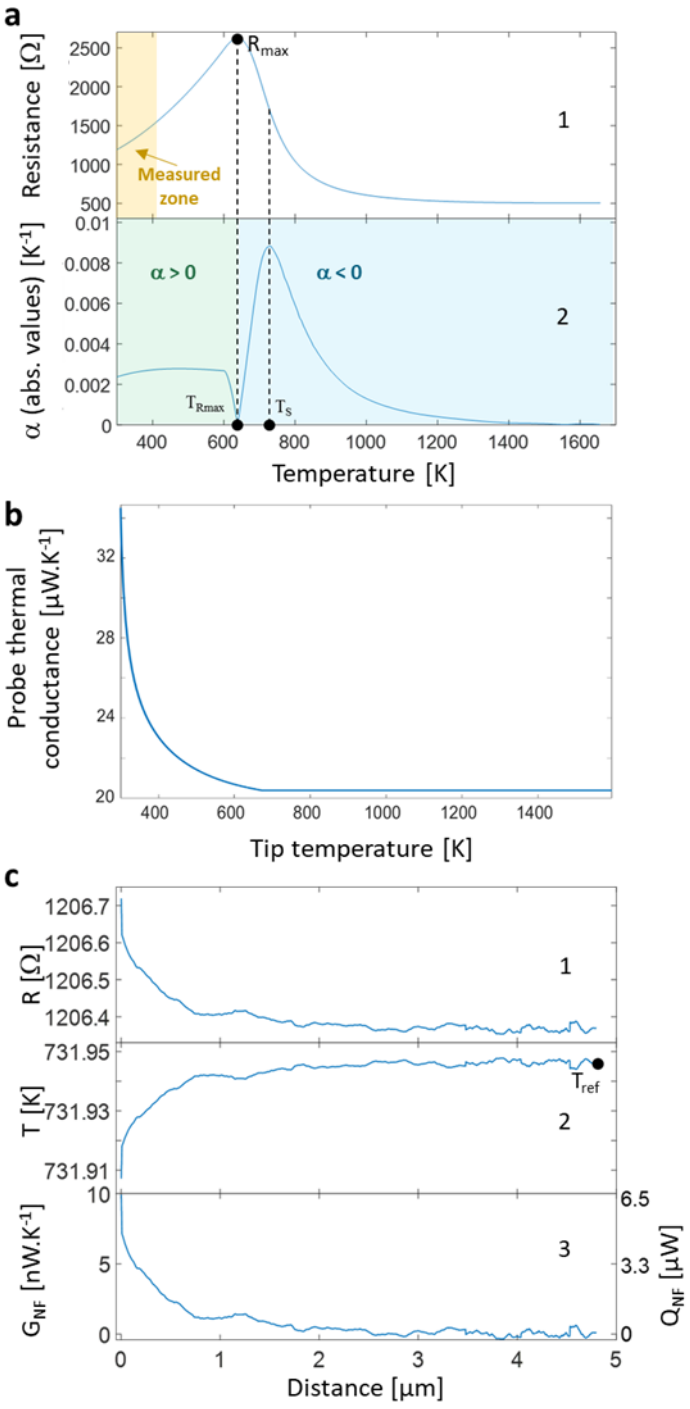

Supplementary Figure 1. Determination of the near-field radiative thermal conductance. (a) Calibration of the emitter temperature: (Step 1) Electrical resistance and (Step 2) temperature coefficient of the electrical resistivity ($\alpha = \frac{1}{R}\frac{dR}{dT}$) of the emitter according to the oven temperature. (b) Total thermal conductance of the probe $G_{tot} = P/\theta$ far from contact in vacuum, as a function of temperature. (c) Application of the calibration for determining the near-field thermal conductance: (Step 1) Electrical resistance, (Step 2) temperature and (Step 3) near-field radiative thermal conductance as a function of distance to the contact. The emitter-sample power exchanged is also indicated. The electrical resistance measurements were averaged over 16 curves.

Temperature measurement of the emitter and near-field thermal conductance

Measurement of the emitter temperature T is needed to determine the radiative heat transfer with the cell characterized by the near-field thermal conductance G_{NF}. The principle is to measure the electrical resistance of the SThM probe R, thermalized with the emitter, and use calibration data to infer its temperature (see above). A Keithley 6221 signal generator was used to provide DC current I to the SThM probe, up to 8 mA depending on the required temperature. A Wheatstone bridge circuit with a 100x voltage amplification was used to accurately measure the electrical resistance. The bridge was balanced with the emitter out of contact, for a distance d slightly smaller than 5 μm, by adjusting the current supply until the electrical resistance of the probe matches the one imposed by a programmable resistance (MEATEST M632) corresponding to the targeted temperature. During the approach, the imbalance of the bridge was measured according to the displacement of the emitter d, and then the electrical resistance R and temperature T were calculated. A Keithley 2182A nanovoltmeter was used to have a direct view of the imbalance of the bridge, while this signal was recorded by means of a NI cDAQ-9178 data acquisition system with a NI 9239 voltage measurement unit at a 2 kHz acquisition rate. For each experiment, up to 100 identical approaches were performed and the resulting curves were averaged to obtain a better signal-to-noise ratio. A sliding average was also applied to remove the 50 Hz electrical noise.

In order to determine the emitter-cell thermal conductance during an approach, we measured the electrical resistance variation of the emitter and used the calibration data to calculate its temperature. The resistance measurements were first averaged before calculating the temperature and the conductance (Supplementary Fig. 1c). Variations of total thermal conductance $G_{tot} = \frac{P}{\theta}$, where P is the electrical power fed to the probe and $\theta = T - T_{amb}$ the average temperature increase, are small. Thus the radiative thermal conductance in the near field G_{NF} , being exactly the variation $\Delta G_{tot}(d)$ which depends on the emitter-cell distance d, can be calculated from a logarithmic derivation: $\frac{\Delta G_{tot}}{G_{tot}} = \frac{\Delta P}{P} - \frac{\Delta \theta}{\theta} = \frac{\Delta R}{R} + \frac{2\Delta I}{I} - \frac{\Delta \theta}{\theta}$. With the reference temperature taken at the largest distance (T_{ref}), the temperature coefficient (α), the emitter current and the reference current at the largest distance (respectively I and I_{ref}), the following equation can be derived:

$$G_{NF} = G_{tot}\left[(T_{ref} - T)\left(\frac{1}{T - T_{amb}} - \alpha\right) + 2\frac{I - I_{ref}}{I}\right] \qquad (1)$$

where G_{tot} is measured at the largest distance (Supplementary Fig. 1b). Depending on the working temperature, α and (I-I_{ref}) are respectively positive/negative for $T < T_{\mathrm{Rmax}}$, and negative/positive for $T > T_{\mathrm{Rmax}}$ because the temperature drop during an approach can result in a decrease or an increase of electrical resistance. In Supplementary Fig. 1c, the temperature drop close to contact is seen as a resistance increase due to the working temperature (≈ 732 K), which is higher than $T_{R\mathrm{max}}$. Finally, it must be noted that G_{NF} is equal to 0 at the largest distances because it represents only the evanescent wave contribution to the radiative heat transfer, which is considered negligible at such distances.

Since radiative measurements can be noisy, they require averaging over many approach curves (see also Supplementary Fig. 1). At room temperature approximately 100 approach curves were considered for averaging. At low temperature (Fig. 3a), seventeen curves were used and consequently the signal-to-noise ratio became small for distances larger than 3 μm (shaded region). The value of the background level was estimated by averaging the measured flux over a distance range of 0.3 μm around the 4 μm position. This sets the main uncertainty on the exact flux determination.

Design and fabrication of the photovoltaic cells

The photovoltaic cells (Fig. 1c) were specifically designed and fabricated to demonstrate the near-field enhancement of the electrical power[3,4]. For the semiconductor material, we chose indium antimonide (InSb) for its low bandgap energy of 0.23 eV (λ_g = 5.3 μm) at 77 K, thus allowing conversion of low-energy infrared radiation (Fig. 1d).
We first analyzed numerically the doping levels and layer thicknesses of the InSb p-n junction to be able to obtain the largest electrical power generation from the cell. Second, we fabricated the optimum cells and measured their photovoltaic response in the far field using different emitter temperatures. Cells were made with different active area diameters of 20, 40, 80 and 160 μm in order to study the influence of the illuminated area on electrical power generation[4]. In order to investigate the impact of cell parameters on conversion performances, two p-doping levels of 10^{17} and 10^{18} cm^{-3}, and two substrate thicknesses of 200 and 500 μm, were selected. The cells were glued with silver paste on a gold-coated chip carrier and connection from the front and back contacts of the cells to the chip carrier was made using wire bonding.
In the present work, we added one step to the previously reported fabrication process[4]. Passivation is required to avoid accumulation of majority carriers at the side walls of the mesa and the associated current that lowers performances of the junction. The extra step consisted in passivating only 20 μm of the circular mesa structure (10 μm from inside of circle and 10 μm from the etched area) by depositing AZ1518 photoresist and then curing it. By means of a plasma-enhanced chemical vapor deposition (PECVD) method at 200 °C, all surfaces, except the cell active area, were then covered with a dielectric material such as SiO_2 or Si_3N_4, which allows preventing shortcuts between contacts and makes it possible to wire-bond. Top views of the resulting cells are shown in Supplementary Fig. 8.

Setup of the experiment

The experimental setup (Fig. 1a, Supplementary Fig. 2a) was assembled in a vacuum chamber with walls at room temperature, where the pressure was decreased to $P \approx 10^{-6}$ mbar, using only an ion pump at that threshold to avoid vibrations. The chip carrier of the cell was glued with silver paste on the cold finger of a liquid-helium cryostat (Supplementary Fig. 2b). The cell position was fixed in the experiment. The emitter was initially placed at approximately 2 mm above the surface of the cell and could be moved in *x*-, *y*- and *z*-axis directions by a custom piezoelectric positioning system having ranges of 3, 3 and 2.5 mm, respectively. Supplementary Fig. 2c shows a closer view of the emitter holder above the cells. Positioning of the emitter above the centre of the active area of the cell was done in three steps. First, the position of the emitter was controlled using piezoelectric positioners and a microscope camera (Dino-Lite Edge 3.0 AM73115MTF) with a long working distance of 15 cm for a 40x magnification located outside the vacuum chamber. The emitter was brought in contact with the chip at an arbitrary location, then retracted at a safe distance of around 100 μm and moved over the cell (see Supplementary Fig. 2d for a top view). In a second step, the emitter was brought in contact with the cell and retracted at a distance *d* smaller than 5 μm. There the fine positioning (step 3) was performed by measuring the short-circuit current (I_{SC}) of the cell according to the emitter displacement along the *x* and *y* axes, with the emitter heated at a temperature larger than 730 K. Once the maximum current is reached along one axis (see Supplementary Fig. 9c), the maximum current position along the other axis corresponds to the centre of the active area. It is reminded that parallelization of the emitter and cell surfaces was not required due to the sphere-plane configuration, chosen on purpose in place of the plane-plane configuration.

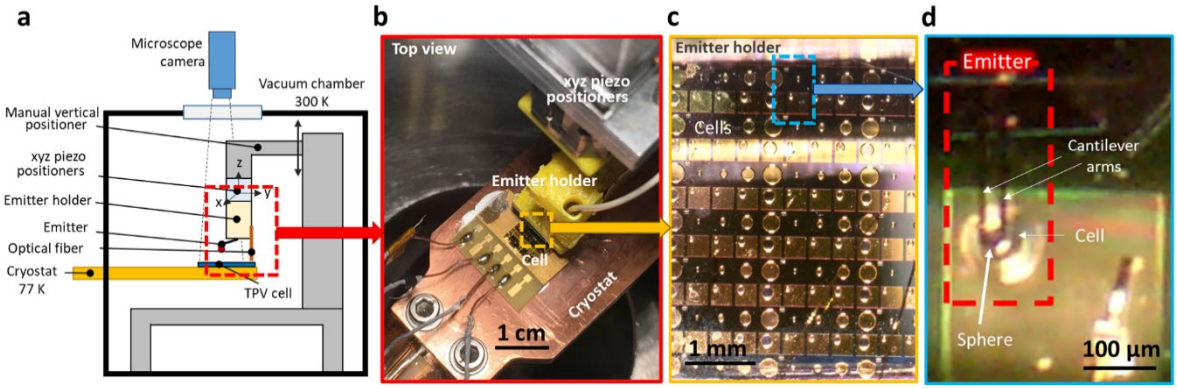

Supplementary Figure 2. General design of the experimental setup. (a) Schematic of the experimental setup. (b) Top view of the main parts of the setup inside the vacuum chamber. (c) Close view of the emitter holder above the TPV cells. (d) Microscope view of the emitter (scanning thermal microscopy probe having a graphite sphere glued on the tip) positioned above a TPV cell.

Detection of contact

The mechanical contact between the emitter and the cell was detected simultaneously by two different methods. The temperature of the emitter was measured continuously according to the piezo displacement. At contact, there is a sudden drop of the temperature due to the contribution of heat conduction which becomes largely dominant over thermal radiation for the heat transfer between the emitter and the cell. The other method was based on the measurement of the cell current according to the displacement of the emitter. When the emitter is in contact, the performances of the cell harshly decrease due to the temperature increase[4] caused by the hot emitter. A significantly-lower photogenerated current is then measured. These two methods applied simultaneously were useful to check that the contact actually occurs in the active area of the cell. When some contact took place with the gold surface sides, the temperature drop of the emitter was still observed but the decrease of the photogenerated current was absent because the heated area does not contribute to the photovoltaic effect. More details on the analysis of the emitter-cell distance is provided in Supplementary Section 6.

I-V characteristics measurement according to emitter-cell distance

The current-voltage (I-V) characteristics of the photovoltaic cells were measured using a Keithley 2400 source measurement unit. A voltage scan was applied to the cell and the resulting current was measured (Fig. 2). For the dark configuration, we used a cooled radiative shield that was mounted around the sample to prevent the active area of the cells from receiving ambient temperature radiation. In order to get the electrical power at the maximum power point according to the emitter-cell distance, I-V curves must be measured as a function of distance. For stability purposes, it was chosen to perform continuous approaches of the emitter while measuring the current produced by the cell for a fixed voltage, and then to repeat this procedure for different voltages. After performing approaches at voltages ranging from 0 to around 140 mV, we obtained a series of current-distance curves at different cell voltages that could be used to plot the current-voltage curves at different distances. Then we calculated the photovoltaic power at each distance and determined the maximum value so as to plot the maximum electrical power according to distance (see Supplementary Fig. 12).

Another method based on the superposition principle is also possible, where the I-V curve of the cell is considered to keep the same shape but is shifted in short-circuit current depending on the illumination level. With this method, a reference I-V curve is measured under ambient illumination, then only the short-circuit current I_{SC} (current at $V_{cell} = 0$) is measured according to distance. The reference I-V curve is then shifted by plotting the (I-I_{SC})-V curves at each distance. Then the maximum electrical power can be calculated. This method is much faster to perform experimentally because it requires approach curves at only one cell voltage, but in this case the maximum power is deduced from the shifted reference curves and not directly measured. Validation of the superposition principle is provided in Supplementary Fig. 10.

Near-field conversion efficiency measurement

The setup allows the simultaneous measurement of the electrical power generated by the cell and the radiative power exchanged between the emitter and the cell in the near field. In order to identify only the near-field contribution to electrical power generation, the theoretical evolution of power according to distance was calculated using the analytical expression of the sphere-disc view factor. We used the electrical power measured at the largest distance in an approach curve similar to Fig. 3b as the fitting parameter, assuming that the generated power was only due to the far-field contribution. The difference between the power calculated with the view factor and the total measured power corresponds to the near-field electrical power. Note that our definition of the far-field contribution is that related to the view-factor theory, and that it can depart from an exact calculation of the contribution of the propagative waves in the selected geometry using fluctuational electrodynamics. In case of a slight error on the identification of the far-field contribution from the experimental data (Fig. 3), our estimation is a lower bound to the near-field contribution. For the different distances, the ratio between the near-field electrical power and the near-field exchanged radiative power gave the conversion efficiency for the near-field contribution only.

2. Selection of the emitter material

In order to choose an efficient emitter material that matches the optical properties of InSb, we performed radiative heat transfer calculations between two semi-infinite planar media labelled 1 and 3 separated by a vacuum gap labeled 2. The spectral heat flux emitted by one of these media at temperature T and absorbed by the second one is the sum of the propagative and evanescent contributions $q = q_{prop} + q_{evan}$ and can be calculated based on the electric properties, here the complex dielectric function ε which depends on the angular frequency ω, of the emitter and the receiver[5]:

$$q_{evan}(\omega) = \frac{1}{\pi^2}\frac{\hbar\omega}{e^{\frac{\hbar\omega}{k_B T}}-1}\int_{k_\parallel=k_0}^{\infty} k_\parallel e^{-2Im(k_{2\perp})d}\sum_{i=TE,TM}\frac{Im(r_{21}^i)Im(r_{23}^i)}{\left|1-r_{21}^i r_{23}^i e^{2ik_{2\perp}d}\right|^2}, \quad \text{(S1a)}$$

$$q_{prop}(\omega) = \frac{1}{4\pi^2}\frac{\hbar\omega}{e^{\frac{\hbar\omega}{k_B T}}-1}\int_{0}^{k_\parallel<k_0} k_\parallel \sum_{i=TE,TM}\frac{(1-\left|r_{21}^i\right|^2)(1-\left|r_{23}^i\right|^2)}{\left|1-r_{21}^i r_{23}^i e^{2ik_{2\perp}d}\right|^2}, \quad \text{(S1b)}$$

We remind that $\hbar\omega$ is the energy of a photon, $k_B$is Boltzmann's constant, and the Fresnel coefficients are defined as:

$$r_{21}^{TE} = \frac{k_{2\perp}-k_{1\perp}}{k_{2\perp}+k_{1\perp}}, \quad \text{(S2a)}$$

$$r_{21}^{TM} = \frac{k_{2\perp}\varepsilon_1-k_{1\perp}\varepsilon_2}{k_{2\perp}\varepsilon_1+k_{1\perp}\varepsilon_1}, \quad \text{(S2b)}$$

where $k_{\parallel}$ is the part of the wavevector $k_0 = \omega/c$ which is parallel to a flat interface and $k_{i\perp} = \sqrt{\varepsilon_i k_0^2 - k_{\parallel}}$. c is the velocity of light. The total net flux is the difference between that emitted by the hot body and absorbed by the cold one, and that emitted by the cold body and absorbed by the hot one.

Different emitter materials were considered at 732 K and coupled with InSb at 77 K. The resulting spectral fluxes are presented in Supplementary Fig. 3a. We observed that in near-field conditions at d = 10 nm, graphite is an excellent emitter because the spectral flux exchanged with InSb is enhanced by more than one order of magnitude compared to the blackbody limit at wavelengths useful for photocurrent generation ($\lambda < \lambda_{gap}$). The integrated flux over such wavelengths according to distance is also studied (Supplementary Fig. 3b). At d > 70 nm, doped silicon is slightly better than graphite but tends to level off at the lowest distances. However, it radiates also much more at wavelengths larger than λ_{gap}, which would result in a higher power output but a lower efficiency than graphite. Graphite was chosen with the aim of studying distances down to the sub-100 nm regime for thermophotovoltaic conversion with the highest efficiency. Ideally, a better emitter material would be supporting surface phonon polaritons at wavelengths close to λ_{gap}(InSb) at 77 K, in order to enhance by several orders of magnitude the radiative heat transfer and the electrical power generation in the near field.

3. Sphere-plane vs. plane-plane configurations

We chose a sphere-plane configuration instead of the plane-plane one to avoid any parallelization issue. A drawback is that the near-field enhancement is strongly reduced since a lower fraction of the emitter area is in the near-field zone compared to a planar one at the same distance (Supplementary Fig. 3d). In order to estimate the radiative flux between a spherical emitter and a semi-infinite planar medium, we used the proximity approximation (PA, also called Derjaguin approximation)[6] for computing the contribution of the near-field flux. A flux database was calculated for the case of the plane-plane geometry from 1 nm to 100 µm for the selected temperature. The principle of the PA is that the spherical shape is approximated as the sum of small planar elements and the sphere-plane flux or conductance can be calculated by integrating the local plane-plane flux weighted by the local perimeter over the half sphere (see schematic in the inset of Supplementary Fig. 3c):

$$G_{sphere-plane}(d,T) = \int_0^{R_{sphere}} G_{plane-plane}\left[\tilde{d}(r),T\right] 2\pi r dr, \qquad \text{(S3)}$$

where $\tilde{d}(r) = d + R_{sphere} - \sqrt{R_{sphere}^2 - r^2}$. We calculated the radiative heat flux between a graphite sphere with diameter 40 µm at 732 K and an InSb plane at 77 K and compared it with a planar emitter having the same surface area (Supplementary Fig. 3d). As expected, the enhancement due to the contribution of the evanescent waves at low distances is much weaker with the spherical emitter (more than one order of magnitude). With a smaller sphere, a larger fraction of the area is in the near-field zone, so the exchanged power value varies more strongly with distance. However, the smaller the sphere, the smaller the exchanged power to be measured. Thus, we chose a diameter of 40 µm as a good compromise between near-field enhancement and power detectability. Consequently, with the sphere-plane geometry, a weaker enhancement of the TPV power in the near field is expected in comparison with the plane-plane geometry.

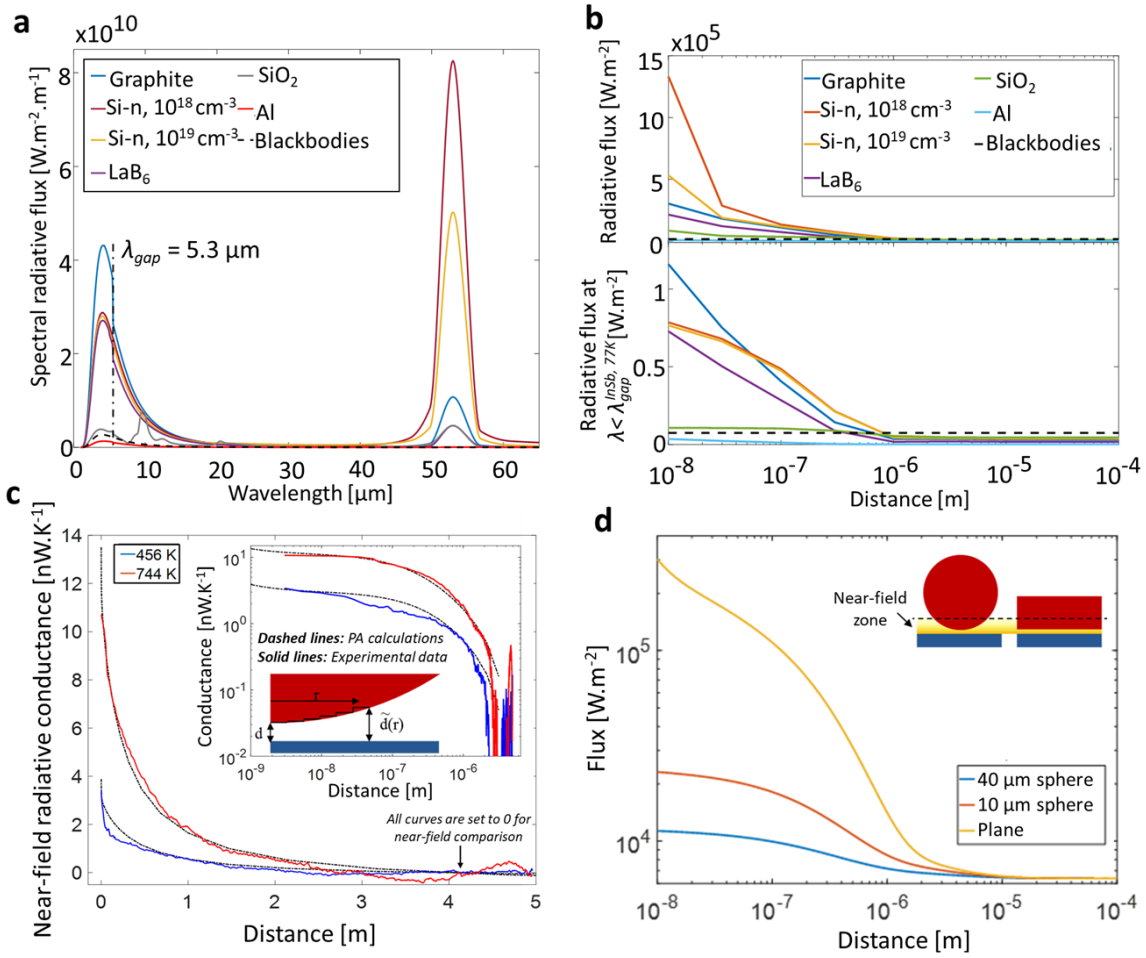

Supplementary Figure 3. Near-field radiative power exchanged for different emitters in the vicinity of semi-infinite planar bodies. (a) Spectral flux between two semi-infinite planar media. Calculations for different emitter materials at 732 K and a sample at 77 K with an emitter-sample distance d = 10 nm. (b) Integrated flux for radiation wavelengths useful for photocurrent generation ($\lambda < \lambda_{gap}$), as a function of distance. (c) Near-field thermal conductance as a function of distance, for two spherical graphite emitter temperatures and a sample at room temperature. Inset: logarithmic plot. Plain lines are experimental data and dashed lines are predictions from the Proximity Approximation. The schematic reminds the principle of the Proximity Approximation (use of the infinite parallel-surfaces heat transfer coefficient and integration as a function of height). (d) Power divided by the projection over the surface area for two different geometries (planar or spherical emitter). The graphite emitter temperature is 732 K and the substrate is at 77 K. The fluxes for the sphere-planar surface geometry are computed by means of the Proximity Approximation.

4. Comparison between near-field thermal radiative measurements and the proximity approximation

Before making measurements with the cells at low temperature, we validated our experimental setup by measuring the near-field thermal radiation exchange at room temperature between different emitters and substrates. Supplementary Fig. 3c reports on measurements between a graphite emitter and a flat InSb substrate. In order to obtain a better signal-to-noise ratio, about 100 approach curves were accumulated and averaged in the present cases. The contact point shifts between the approaches due to some long drift and is therefore tracked before averaging the data by searching for the distance where the electrical resistance varies abruptly. The effect

of the emitter temperature can be observed: the near-field radiative conductance increases by half a decade when the emitter temperature is varied from 456 K to 744 K.

A comparison with the prediction of the Proximity Approximation (Eq. (S3)) is also shown in Supplementary Fig. 3c. It is observed that there are some little differences, ascribed to the fact that the Proximity Approximation is more accurate at small distances than at micrometer-scale ones. At very small distances (in the sub-200 nm regime), where the position is determined less accurately (see Section 7), a lower slope is observed in the logarithmic plot for both the experimental data and the predictions.

5. Contribution of the propagating modes with distance

The far-field radiative flux was estimated based on two different approaches. First, the macroscopic theory of view factors was used by assuming diffuse isotropic surfaces. The analytic expression of the sphere-disc view factor depending on the cell and sphere radii R_{disc} and R_{sphere}, and the sphere-cell distance d, reads as follows[7]:

$$F_{s\to d} = \frac{1}{2}\left(1 - \frac{1}{\sqrt{1+\left(\frac{R_{disc}}{d+R_{sphere}}\right)^2}}\right) \quad \text{(S4)}$$

Due to the flatness of the surfaces, it could be argued that the surfaces are specular and not diffuse. A second method was then implemented, using a Monte Carlo ray tracing numerical approach (see principle on Supplementary Fig. 4a). For precise calculations, we considered the properties of graphite and the materials constituting the InSb cell, such as emissivity and reflectance, as a function of emission angle. In this method, rays are launched from the emitter into all directions. A fraction of the total power emitted by the sphere is attributed to each ray depending on the spectral distribution of the radiative flux at the emitter temperature. Then calculations are made to check if the rays coming from the sphere are crossing the surface of the cell. If so, the trajectory is extended by considering the angle of incidence, and the power lost by the ray (absorbed by the cell) is calculated using the reflectivity of InSb. Then we check if the extended trajectory crosses the surface of the sphere. Using the same principle as before, the power loss and the reflected trajectory are calculated. In this method, we considered up to 3 reflections on the sphere for the same ray, because it was estimated that the number of remaining rays and their energy after such a number of reflections were negligible. The results of the Monte Carlo method which are shown are for a spherical emitter with diameter of 40 µm and a finite disc with different diameters as the receiver. The total flux absorbed by the disc, which is representative of the cell, is provided by a map of the power density (Supplementary Fig. 4b) and a power density profile integrated as a function of cell radius (Supplementary Fig. 4c). We observe in the figures that the flux decays for radii larger than 20 µm, so it is not necessary to use cells with a too large radius as most of the surface would not be much illuminated by the sphere. We could also calculate the evolution of the radiative power deposited on the cell as a function of distance (Supplementary Fig. 4d). We can see that for distances smaller than ≈ 3 µm, variations of the flux are very small so most of the measured enhanced power will be coming from the contribution of the evanescent waves in the near field. We compared the Monte Carlo simulations of the specular bodies considering 10^6 rays with the analytical expression of the diffuse-emission view factor and found a very good agreement between the results. The specularity of the surface is therefore not key to the computation of

the exchanged power. Taking into consideration this result and because the Monte Carlo simulations need a significant computational time, the propagating mode contribution was calculated for a single distance using the Monte-Carlo method. The flux at other distances was deduced from both this value and the analytical expression of the view factor. Note that the reflectance of the cell, which is a multilayered structure, were first calculated by electromagnetic means and then included in the Monte Carlo approach for the estimation of the propagative-wave contribution (see Supplementary Fig. 4e).

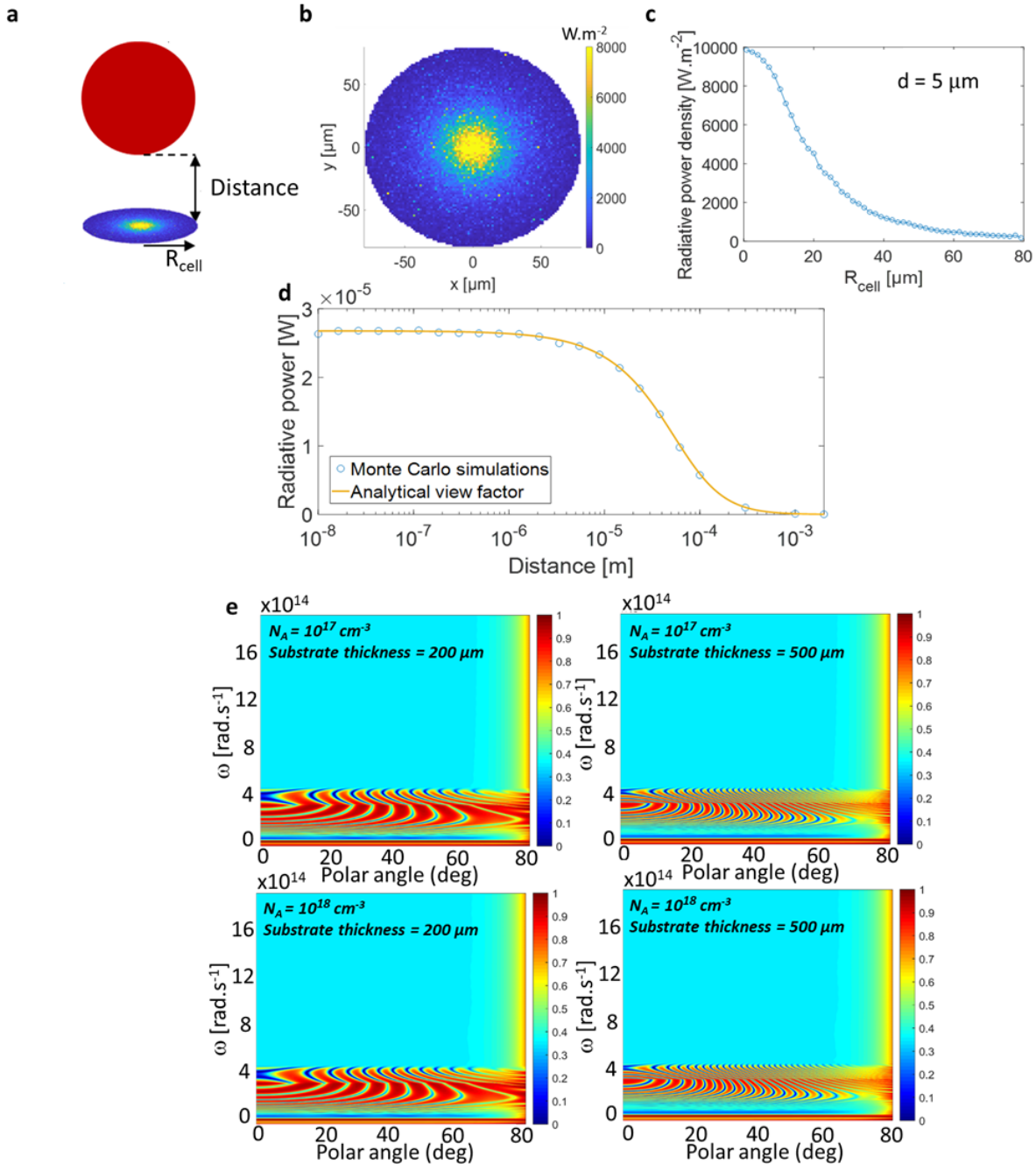

Supplementary Figure 4. Calculations of the contribution of the propagative waves to the radiative power according to distance. (a) Schematic of the Monte Carlo computation of the propagative photon contribution to the transfer between the hot sphere and the cold receiver. (b) Local radiative power density deposited by a 40 µm graphite sphere at 732 K on a flat InSb semi-infinite cylinder of diameter 160 µm at 77 K, for an emitter-cell distance equal to 5 µm. The cylinder represents the cell. (c) Radiative

power density as a function of cell radius. (d) Evolution of the radiative power calculated using the view factor as a function of distance, compared with the Monte Carlo simulations. (e) Spectral and directional specular reflectance of an InSb cell extended infinitely in the lateral directions and consisting of four layers (p-doped, $N_A = 10^{17}$ or 10^{18} cm^{-3}, $t_p = 0.5$ µm / n-doped, $N_d = 10^{15}$ cm^{-3}, $t_n = 2.5$ µm / n-doped substrate, $N_{d,sub} = 4\ 10^{17}$ cm^{-3}, $t_{sub} = 500$ or 200 µm / gold, $t_{brl} = 200$ nm). These data, computed by electromagnetic means, are inputs in the Monte Carlo computation of the far-field contribution.

6. Numerical analysis of the near-field modes and radiative absorption as a function of depth

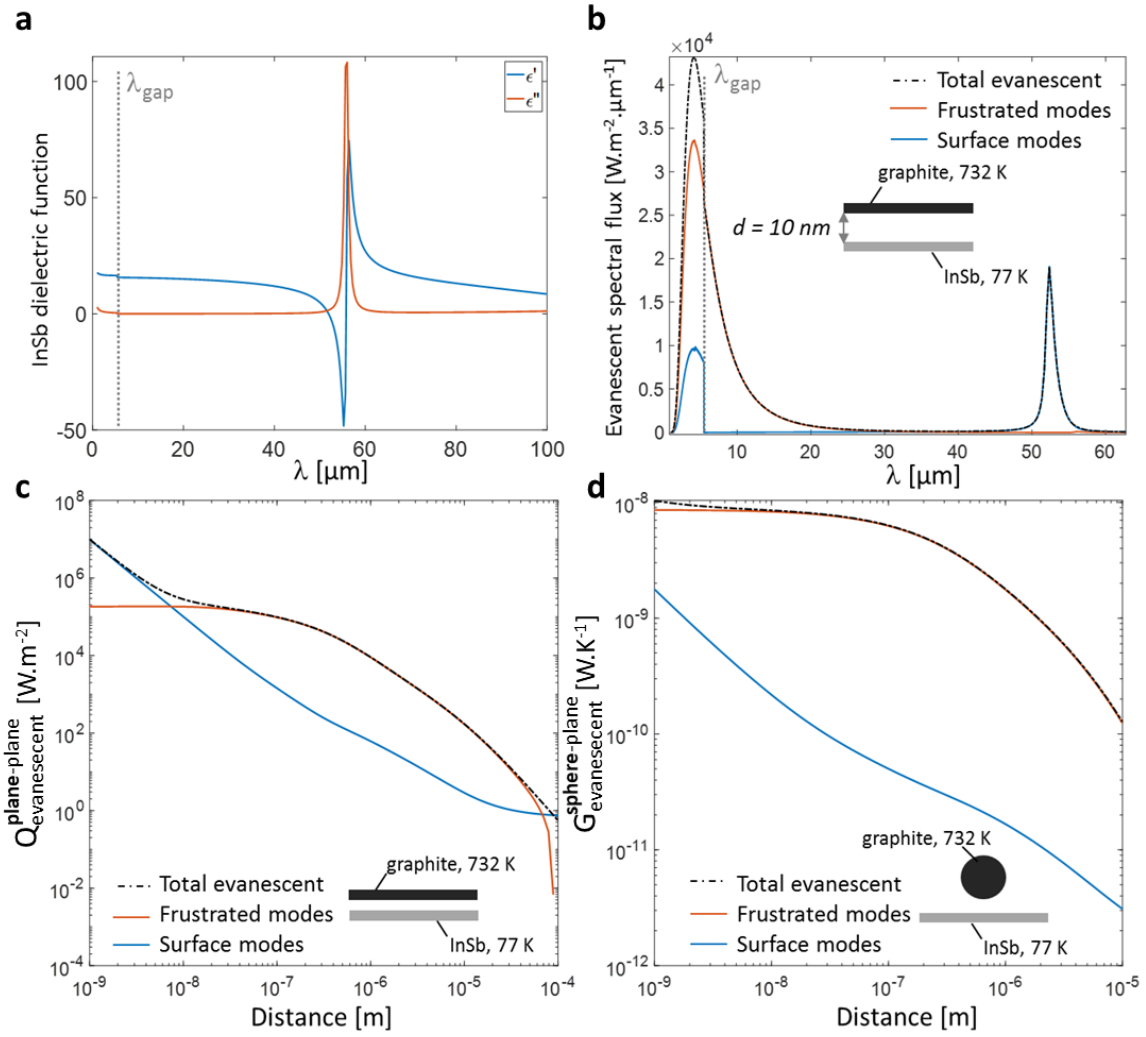

Supplementary Figure 5. Contribution of the frustrated and surface modes to the evanescent radiative heat transfer. The emitter temperature is 732 K and the InSb semi-infinite planar medium receiver is at 77 K (a) Real (blue) and imaginary (red) parts of the dielectric function of InSb at 77 K (p doping level of 10^{18} cm^{-3}). (b) Evanescent component of the spectral flux between two semi-infinite planar media separated by a 10 nm vacuum gap. (c) Evanescent flux as a function of the distance between two semi-infinite planar media. (d) Evanescent conductance as a function of distance, for a 37.5 µm graphite sphere and an InSb semi-infinite planar medium.

It is key to study the contribution of the different evanescent modes to the heat flux, *i.e.* frustrated and surface modes. Frustrated modes undergo total internal reflection at an interface, they are propagative in the medium and evanescent in vacuum. Surface modes are evanescent both in vacuum and in the medium. The dielectric function of InSb (Supplementary Fig. 5a)

allows for resonant surface waves (phonon-polaritons) around the wavelength $\lambda = 55$ µm, which is by far larger than the wavelength corresponding to the bandgap of InSb at 77 K (5.3 µm) and λ_{Wien} (3.96 µm at 732 K).

We consider a semi-infinite medium of InSb as the receiver. We first analyze the plane-plane configuration. In Supplementary Fig. 5b, computed for $d = 10$ nm (a very small distance with respect to possible applications), we observe a peak in the spectral flux around 55 µm due to the phonon-polariton of InSb. The distance dependence shows that the evanescent component of the radiative heat transfer is dominated by the frustrated modes for approximately $d > 40$ nm (Supplementary Fig. 5c). For the sphere-plane configuration (Supplementary Fig. 5d), this translates into a domination of the frustrated modes for distances $d > 10$ nm. Knowing the uncertainty on distance close to the contact (see Section 6), this study indicates that, in our case, the near-field radiative heat transfer is fully dominated by the frustrated modes. The surface modes do not contribute to the electrical power generation by the cell in our experiment.

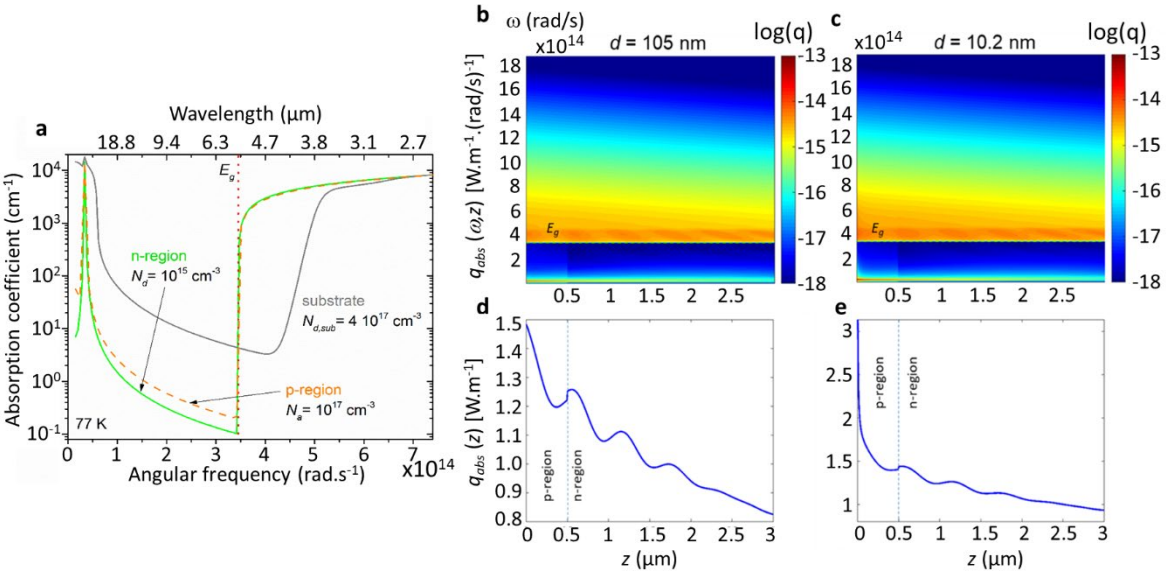

Supplementary Figure 6. Radiative power absorbed as a function of frequency and depth, for sphere-cell distances of 105 nm (b,d) and 10.2 nm (c,e) and a substrate thickness of 500 µm. (a) Spectral absorption coefficient of indium antimonide (a) and (b) penetration depth for different doping levels considered for these calculations. (c,d) Local spectral radiation power absorbed as a function of depth (z) inside the cell. (e,f) Local radiation power absorbed as a function of depth. The results are computed with the Proximity Approximation for both evanescent and propagative contributions, and with the following parameters: graphite sphere of diameter 40 µm at 773 K, InSb cell at 77 K made of four layers (p-doped, $N_a = 10^{17}$ cm^{-3}, $t_p = 0.5$ µm / n-doped, $N_d = 10^{15}$ cm^{-3}, $t_n = 2.5$ µm / n-doped substrate, $N_{d,sub} = 4\ 10^{17}$ cm^{-3}, $t_{sub} = 500$ µm / gold, $t_{brl} = 200$ nm). Surface modes decay quickly from the surface at $d = 10$ nm, and are not present at 100 nm.

Let us now move to actual geometries and materials. The dependence of the dielectric function on doping concentration is reminded in Supplementary Fig. 6a. The absorption coefficient of InSb is calculated[3] at 77 K for the p-region ($N_a = 10^{17}$ cm^{-3}) in the standard configuration used in the core paper, the n-region ($N_d = 10^{15}$ cm^{-3}), and the n-doped substrate ($N_{d,sub} = 4\ 10^{17}$ cm^{-3}). Some differences can be seen below the bandgap, where the doping has a strong influence. The penetration depth (Supplementary Fig. 6b) just above the bandgap is large, and the substrate is even more transparent. The spectral heat flux absorbed as a function of position in

the cell is reported in Supplementary Figs. 6c and 6d. It is computed with the Proximity Approximation (see Secs. 3-4) and the methods described in Ref. 4. Note that in contrast to other sections, the PA is also applied here for the propagative contribution, which is a stronger approximation but allows obtaining an estimation of the absorption as a function of depth. At a distance of ~100 nm (Supplementary Fig. 6c), which is close to the minimum one achievable in our experiment (see Section 6), all the power absorbed in the junction (first 3 μm from the top of the cell, see Fig. 1 for the whole architecture) is located above the bandgap and there is no contribution of the polariton as suggested by Supplementary Fig. 5d. Some interference patterns are observed in the junction. The power absorbed decays slowly as a function of depth, which calls for the introduction of a mirror as close as possible from the junction to allow for a second passage of the photons that have not been absorbed. We remind that the electron-hole pair generation rates are a direct translation of the absorbed power in the junction above the bandgap.

Let us now analyze smaller distances ($d \sim 10$ nm), which may be more difficult to implement in practical applications. Now the contribution of surface modes, which decay quickly from the surface, can be observed (Supplementary Figs. 5c and 5d). Exploiting these modes requires positioning the n-p contact region close to the top surface and induces addition constrains. While this distance regime was not tested experimentally, our design is compatible with it.

7. Estimation of the sphere-cell distance close to contact

a) Effect of the attraction forces

The distance when the sphere is few nanometers close to contact can also be modified by the attraction forces between the sphere and the surface. These forces are expected to bend the SThM probe cantilever and thus bring the sphere into contact. In order to quantify the distance where the snap-in occurs, we performed cantilever deflection measurements as a function of distance at room temperature for different emitter temperatures. The deflection was measured with a photodiode system in an NTMDT atomic force microscope (AFM) equipped with a moderate-vacuum chamber (10^{-1} mbar). In this experiment, a laser was focused on the edge of a SThM probe with a sphere glued on the tip, and the reflection of the laser was observed with a quadrant photodiode. The cantilever deflection δz could be measured by looking at the δx displacement of the reflected laser on the photodiode (Supplementary Fig. 7a). In out-of-contact position, the deflection of the probe is constant because there is no interaction between the probe and the sample. In the approach curve close to contact (Supplementary Fig. 7b), the cantilever bends slightly due to the attraction forces. We estimated this bending to be around 2-3 nm. Thus, it corresponds to a distance range not achievable with this experimental configuration. It can also be noticed that the adhesion forces, taking place when the probe is withdrawn, lead to a much larger deflection, greater than 20 nm.

b) Effect of roughness

At low distances, the effect of surface roughness can become important. We performed roughness measurements both on the sphere and the cell using atomic force microscopy to acquire topographic images. By using the same principle as before, the deflection of an AFM probe was measured when the surface of the sample was scanned is xy directions. The root-mean-square roughness R_{RMS} and more importantly the maximum peak height and valley depth were determined from these measurements. For the sphere, an additional data processing was necessary as the surface is not flat: a spherical shape with the corresponding radius of curvature was subtracted from the measured data to obtain a flat topographic image (Supplementary Fig.

7c). We found that the cells were almost perfectly flat with R_{RMS} = 0.2 nm whereas the graphite spheres had R_{RMS} = 5.2 nm with +29.9 nm and -28.7 nm as peak height and valley depth, respectively. These values mean that when we considered the sphere to be in contact with the cell for $d = 0$, the effective distance is most probably $d \approx 30$ nm between the surface of the cell and the mean spherical shape. This indicates that the study is restricted to distances larger than 30 nm.

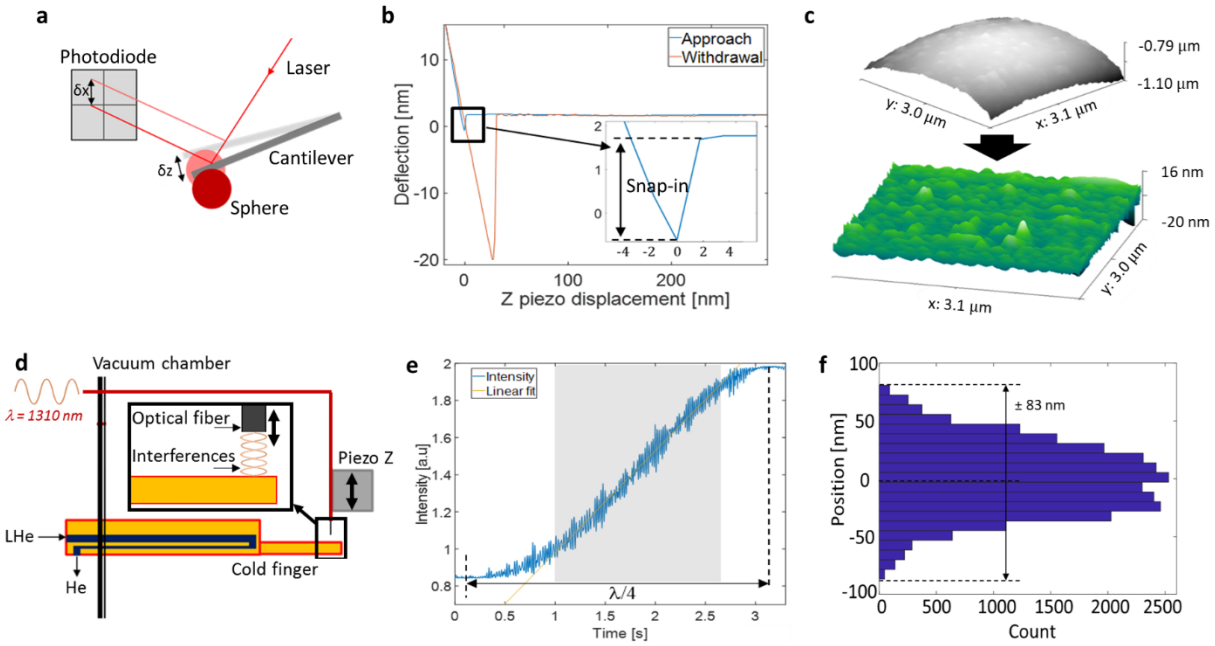

Supplementary Figure 7. Parameters influencing the determination of the emitter-cell distance at contact, *i.e.* the snap-in distance associated to the jump at contact (a,b), the sphere material roughness (c), and sample vibrations (d-f). (a) Schematic of the cantilever deflection measurement setup using a quadrant photodiode system. (b) Cantilever deflection as a function of the displacement during an approach (blue) and a withdrawal motion (red). The emitter is out of contact when the curve is flat and is in contact when the slope is steep. The data indicate an uncertainty of few nanometers at maximum. (c) Topographic image of the sphere obtained by scanning the emitter with an atomic force microscopy tip, before and after spherical shape subtraction. This allows determining the roughness of the emitter involving a rms roughness of 5 nm and peaks of maximal height around 30 nm. (d) Schematic of the interferometric vibration measurement setup allowing to measure the variation of position of the cell with respect to the cantilever basis. (e) Interferometric signal allowing to calculate the vibration amplitudes. The linear domain is represented by the shaded area. (f) Histogram of the cold finger positions, indicating a maximal vibration amplitude of about 80 nm.

c) Vibrations of the cryostat

In order to cool the cells down to 77 K, we used a liquid helium (LHe) cryostat with a cold finger located inside a vacuum chamber (LHe was used for practical reasons but liquid nitrogen can also be used). The cold finger is 15 cm long inside the vacuum chamber so the continuous flow of LHe in the finger induces mechanical oscillations. In our case it is very important to know the amplitude of these vibrations because it corresponds to the minimum achievable emitter-cell distance. We used an Attocube LDM1300 interferometric module based on an IR laser with a 1310 nm wavelength fed through an optical fiber in order to measure the amplitude of the vibrations. The fiber was attached to the setup on the *z*-piezo where the emitter is usually located during the experiments, and was placed close to the surface of the cold finger (see Supplementary Fig. 7d). Then we moved the fiber at a constant speed over a 5 µm range by doing a series of approach/withdrawal motions while the periodic interferometric signal was

acquired. When the fiber moves by a distance λ corresponding to the wavelength of the laser, the optical path is modified by 2λ so the period of the interferometric signal corresponds to a λ/2 displacement. We can deduce the signal for half a period corresponding to a λ/4 = 327.5 nm displacement and find a local linear fit for the data (Supplementary Fig. 7e). Knowing the displacement and the moving speed of the fiber, we can easily establish a relation between the intensity of the signal and the displacement, and calculate the vibrations amplitude around the average position given by the linear fit by looking at the histogram of the positions of the cold finger (Supplementary Fig. 7f). We measured oscillations of the cold finger around the mean position of ± 83 nm. In the experiment performed at low temperature, the impact of the roughness of the sphere combined with the vibrations of the cryostat induce therefore a strong distance uncertainty in the sub-100 nm regime.

8. Characterization of the photovoltaic cells

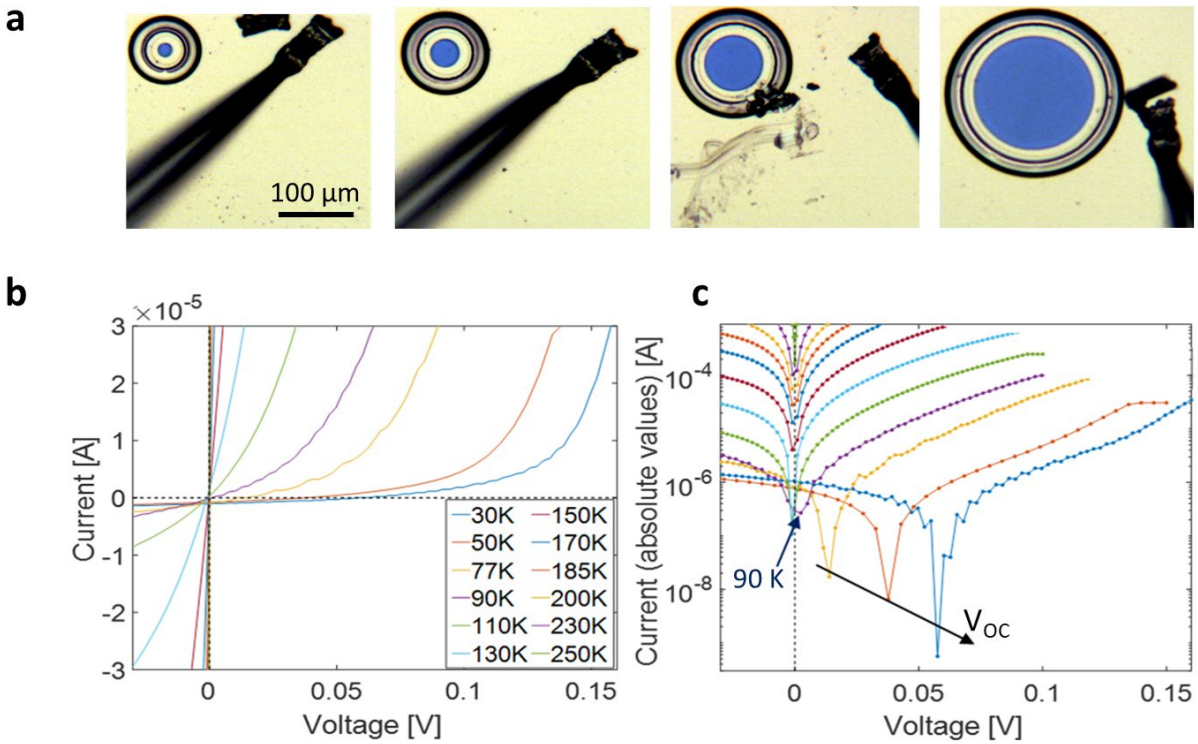

Supplementary Figure 8. Pictures and I-V characteristics of the cells. (a) Top view of the InSb photovoltaic cells with different active area diameters. (b) I-V characteristics at different temperatures. (c) I-V characteristics at different temperatures with the current represented in absolute value and using a logarithmic scale.

The fabricated photovoltaic cells (see Main experimental methods) are shown in Supplementary Fig. 8a. Because the cells are made of InSb, a very low energy bandgap material, they need to be cooled to operate properly[4]. In order to verify this requirement, we performed I-V curve measurements in the dark for different cell temperatures from 30 K to 250 K (Supplementary Fig. 8b). In this configuration, thermal radiation illuminating the cell comes only from the ambient-temperature environment. Above ~110 K, the I-V characteristics are linear. They do not correspond to a diode behavior anymore but are those of a passive resistive device. In this case the thermally-generated carrier concentration is high and the p-n junction effect does not exist anymore. When temperature decreases the exponential shape of the curve

progressively appears. The reverse bias current rises while the forward bias current decreases. We observe in the semi-logarithmic scale (Supplementary Fig. 8c) that for $T \leq 90$ K, the open circuit voltage (V_{OC}) becomes positive and keeps increasing when the cell temperature is decreasing. The presence of a positive V_{OC} means that the cell is generating power due to the 300 K ambient illumination. Thus, the cell needs to be cooled to work properly. For our experiments, we chose a working temperature of 77 K as it corresponds to the commonly-used boiling point of liquid nitrogen. In addition, the illumination level provided by the emitter is high so the generated current is large enough to be detected at this temperature and does not require a lower temperature cooling to reduce the dark current. Note that in the main text (Fig. 2), it can be seen that the I-V characteristics in the dark exhibits a slightly-positive value for the short-circuit current. This is due to a slight offset of the electronics (2-3 nA), which was not subtracted in the results presented in the article.

The I-V characteristics indicate low series resistance in the devices. This is especially possible for micron-sized photovoltaic cells. However, the series resistance losses raise with current, which would become huge in large area photovoltaic cells. Smart designs of the front electrode have been recently discussed in this respect[8,9] and could help in upscaling.

9. Experimental results in the far field showing excellent agreements with the sphere-disc view factor

The experimental setup allows the measurement of the short-circuit current of the cell for emitter-cell distances up to 2 mm. In order to analyze the contribution of the far field to the photocurrent generation, we measured the short-circuit current (I_{SC}) of a cell having a 20 µm diameter active area with the emitter moving from the contact up to $d > 150$ µm, where the current starts to level off due to the low illumination. In this case, we used the *z*-piezo positioner in slip-stick mode with 80 nm steps. Then we compared the measured data to the evolution predicted by the analytic expression of the sphere-disc view factor given in Eq. (S4). Supplementary Fig. 9b (same data as that in the inset of Fig. 3b, different experiment than that reported in the other panels of Fig. 3) shows that the evolution of the short-circuit current matches well the prediction of the view factor from a few micrometers to more than 150 µm. This analysis shows that the far-field thermophotovoltaic conversion efficiency does not depend on distance. Below 2-3 µm, the measured data and the view factor prediction are not in agreement because the evanescent waves are contributing to the radiative heat transfer in addition to the propagative wave contribution predicted by the view factor (insets, Supplementary Fig. 9b and Fig. 4b).

We also measured the evolution of I_{SC} as a function of the lateral displacement of the emitter along the *x* or *y* axis, as it is the main parameter used to accurately position the emitter above the center of the active area of the cell (Supplementary Fig. 9c). In this example the hot emitter was placed at $d \approx 10$ µm from the cell surface and was moved laterally from approximately -120 µm to +120 µm relative to the center of the cell, while the short-circuit current was measured. As expected we observed a maximum for the current when the emitter is above the center (see optical-microscopy view from top in Supplementary Fig. 9a), which first decreases rapidly and then more smoothly as the emitter goes away from the center. The measurements are shown in Supplementary Fig. 9c, together with the theoretical model using the view factor, with a normalization applied at the maximum value. It can be noted that the measurements are slightly non-symmetrical. This issue is mainly due to the fact that the motion of the *x* and *y* positioners is not always perfectly smooth and linear, and can vary slightly over large

displacements (larger than 100 µm). Most importantly, performing this kind of measurement along both x and y directions for a lower displacement range (approximately the size of the active area) provides a precise positioning of the emitter above the center of the cell. This is performed at vertical distances lower than 5 µm.

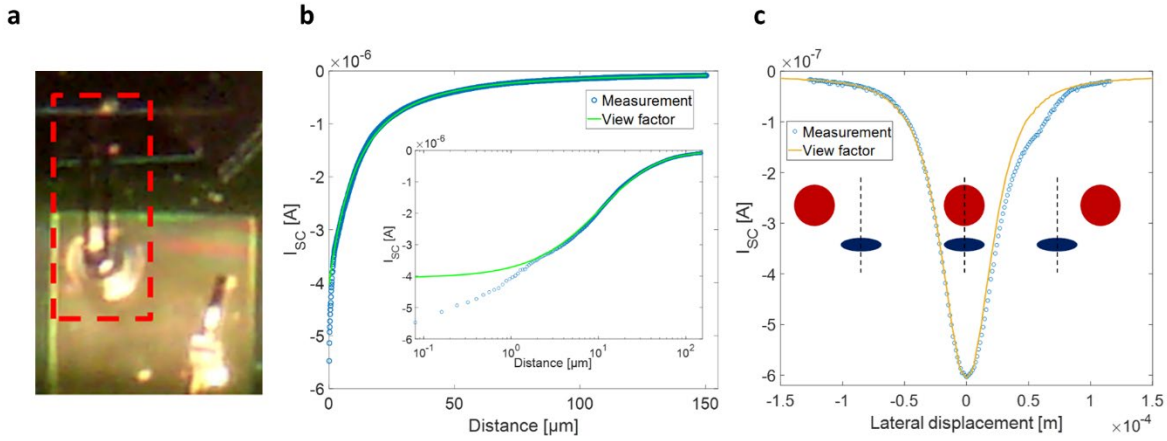

Supplementary Figure 9. Variations of the short-circuit current as a function of position of the emitter. (a) Optical microscopy image of the setup involving the chip where a thermophotovoltaic cell (disc where there is no gold) is seen. Red box: View from top of the scanning thermal microscopy probe on which the spherical emitter is glued, positioned over a cell. (b) Short-circuit current as a function of the vertical displacement of the emitter and comparison with the view factor. Same data as that of the inset of Fig. 3b, but in linear scale. (c) Short-circuit current as a function of the lateral displacement of the emitter and comparison with the view factor.

10. Validation of the superposition principle

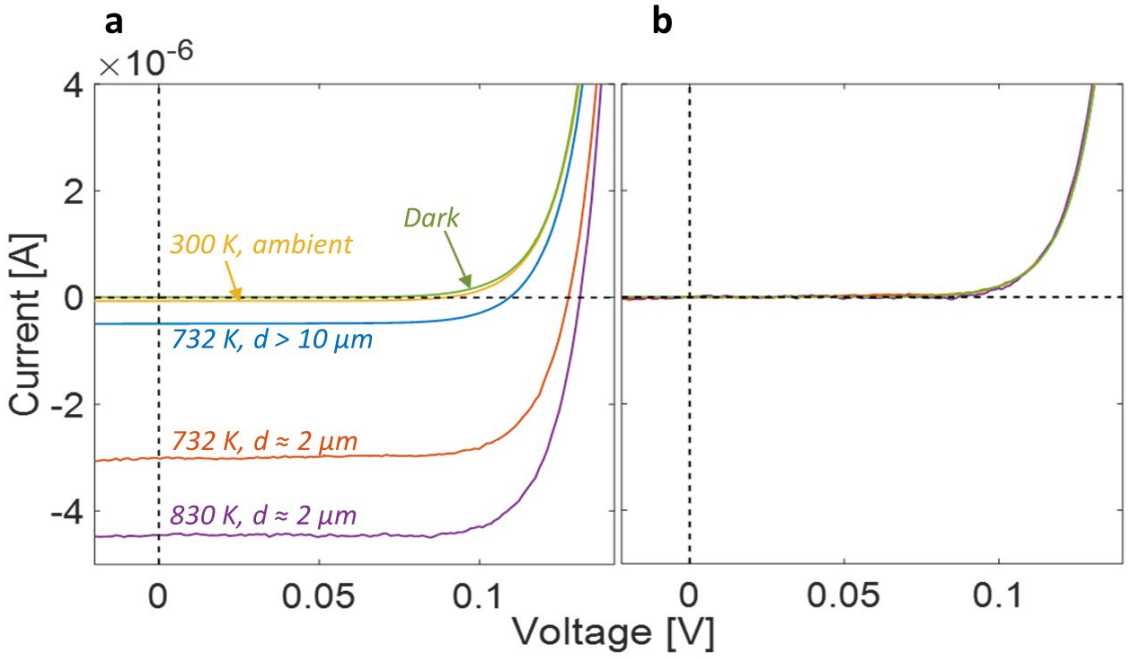

Supplementary Figure 10. I-V curves of a cell having a 20 µm active area diameter in the dark and under different illumination levels. (a) I-V curves under illumination from different distances and temperatures. (b) Curves shifted in current: the short-circuit current of each curve is set equal to zero. All curves superimpose, as expected from the superposition principle.

For photovoltaic cells, the superposition principle tells that the measured photocurrent is equal to the sum of the current generated in dark conditions and the short-circuit current under illumination[10] in low-injection conditions[11]. So, theory suggests that the shape of the I-V curve remains the same and is just shifted in I_{SC} depending on illumination. This principle is very interesting experimentally because the entire I-V curve could be retrieved by measuring only the curve in the dark and then measuring I_{SC} as a function of illumination. In order to verify the superposition principle, we started by measuring the I-V curve of a cell having a 20 µm active area diameter under dark conditions with a cooled radiative shield over the active area of the cell to block the ambient radiation coming from the environment. Then we used the emitter to provide different levels of illumination to the cell by either changing the emitter-cell distance or the emitter temperature (Supplementary Fig. 10a). As expected we observed that when illumination increases the I-V curves are lowered into the photogeneration quadrant, corresponding to larger I_{SC} and V_{OC}. It is worth noticing that the fill factors range from 0.69 to 0.75 at the highest illumination, which is remarkable for a cell with a low bandgap. Then we shifted each curves in current only so their I_{SC} were all set equal to 0 (Supplementary Fig. 10b). We observe that all the curves are well superimposed, so the superposition principle is valid for this kind of TPV cell. The fact that the superposition principle is valid is a proof that the temperature of the cell remains the same (77 K). Since the shape of the I-V curve strongly depends on temperature (see Supplementary Figs. 8b and 8c), the curves would not be superimposed if the cell temperature was modified.

11. Impact of emitter temperature on power output

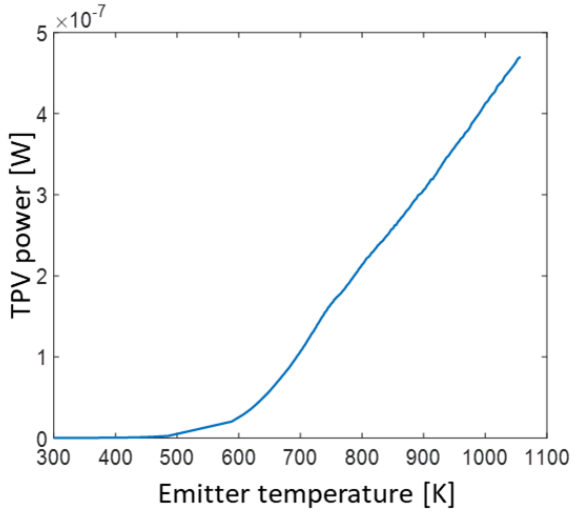

Supplementary Figure 11. Impact of the emitter temperature on the near-field thermophotovoltaic (TPV) power output, measured at d ≈ 5 µm for a photovoltaic cell having an active area diameter of 20 µm.

Although the melting point of InSb is 800 K, it was possible to make experiments with the emitter heated beyond this temperature (≈900 K) without degrading the cell at contact, most probably because the thermal contact resistance between the emitter and the cell limits the cell heating at contact. When the emitter is too hot, however, the cell can be locally heated at $T >$ 800 K in the contact region. An attempt made with an emitter at ≈1200 K led to a degradation of the cell. As a consequence, we know that the threshold for the contact between the emitter and the cell is for an emitter temperature between 900 K and 1200 K. This issue does not

prevent possible measurements with very hot emitters close to the cell, however the exact distance separating them cannot be measured easily with our method (see Supplementary Fig 11). Note that the uncertainty on temperature becomes large at the high temperatures.

12. I-V characteristics and efficiency according to distance

We studied parameters such as the thickness of the cell substrate, the diameter of the active area and p-doping level of the top layer. In Supplementary Fig. 12, we provide the I-V characteristics reconstructed from the approaches at constant voltage for different cells.
By selecting the maximum power for each cell and conditions, this allows to plot the power output as a function of distance (Supplementary Fig. 13). Since we measure also the near-field radiative exchange (Supplementary Fig. 13, middle figure for each set of parameters), we can deduce the near-field efficiency for all set of parameters in a way similar to that of Fig. 3 of the main manuscript.

Supplementary Fig. 14 also provides other types of efficiencies as a function of distance for a particular cell. The red curve corresponds to the measured near-field efficiency, as in Fig. 3 of the core manuscript and those shown in Supplementary Fig. 13.
The total efficiency, which is calculated by adding the estimation of far-field power exchanged to the actual measurement of the near-field thermal radiative power (or the near-field calculation by means of the Proximity Approximation, see previous sections, as measured and calculated data are close), can be deduced. The black curve results from the ratio of the measured electrical power P_{Max} generated by the cell divided by the calculated radiative power absorbed by the cell (near-field: $Q_{NF,calc}$ calculated with the proximity approximation; far-field: $Q_{FF,calc}$ calculated with the Monte Carlo method).
Since only the photons with energies larger than the bandgap are converted, we also analyze the efficiency above the bandgap (yellow curve). This curve is therefore the estimated efficiency considering only photons absorbed at $\lambda < \lambda_{gap}^{InSb,\ 77\ K}$.
Finally, photons with energies much larger than the bandgap are not able to provide all their energy for conversion. As a result, we calculate the number of electron-hole pairs collected by the cell and divide them by the number of photons above the bandgap, which allows determining the share of useful converted photons (purple curve). The purple curve is therefore the estimated efficiency of electrical charge generation and is equal to the number of charges generated and collected by the cell ${P_{Max}}/{qV_{Max}}$ (with q the elementary charge and V_{Max} the measured voltage at the maximum power point) divided by $\int_{\omega_{gap}^{InSb,\,77K}}^{+\infty} \frac{q_{NF,calc}(\omega)}{\hbar\omega} d\omega + \int_{\omega_{gap}^{InSb,\,77K}}^{+\infty} \frac{q_{FF,calc}(\omega)}{\hbar\omega} d\omega$ corresponding to the number of photons absorbed at $\lambda < \lambda_{gap}^{InSb,\ 77\ K}$.

This analysis establishes that the cell is very efficient, especially for near-field photons as conversion rates larger than 70-80% are reached.

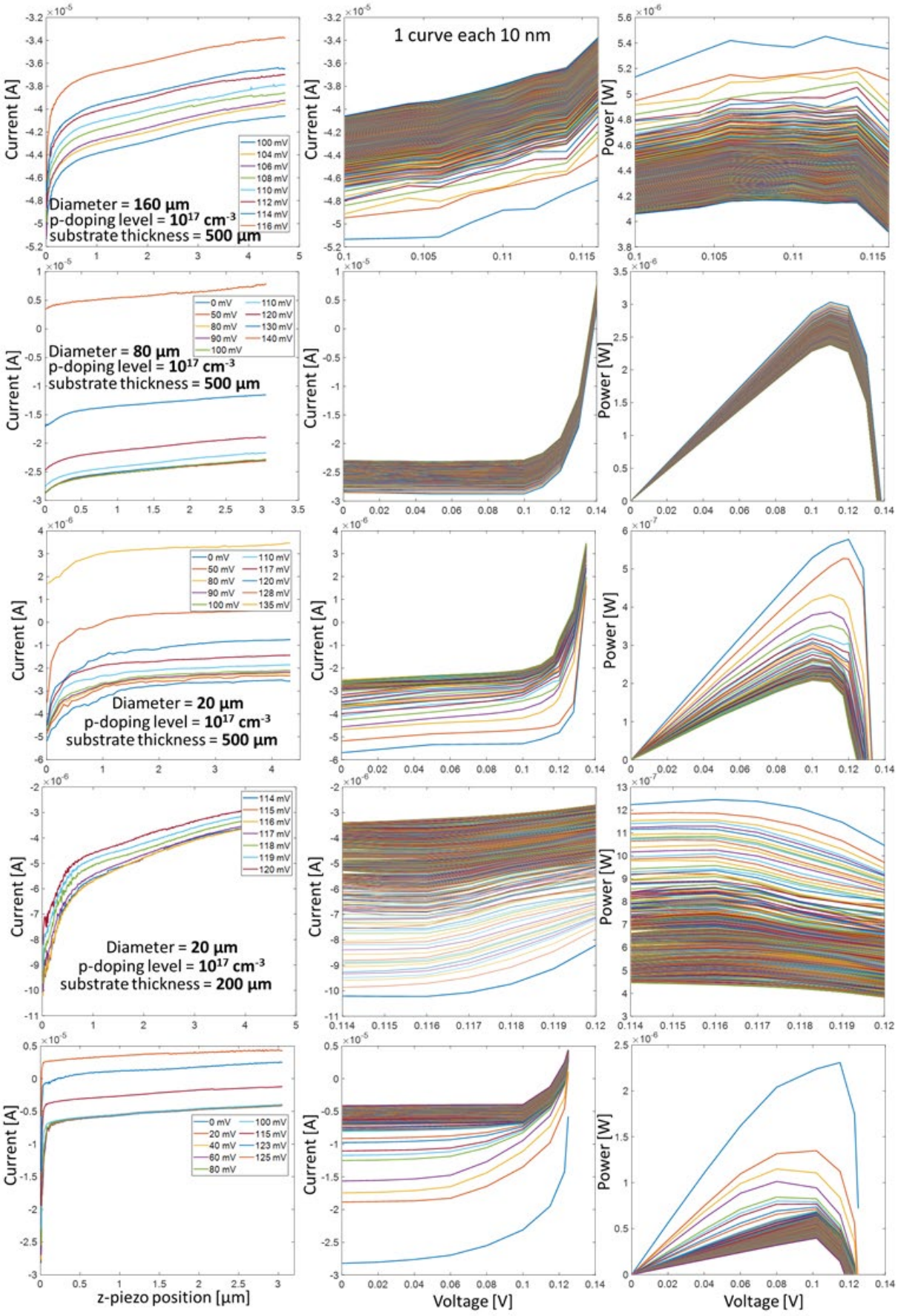

Supplementary Figure 12. I-V characteristics and electrical power generated by the cells measured during the near-field thermophotovoltaic experiments.

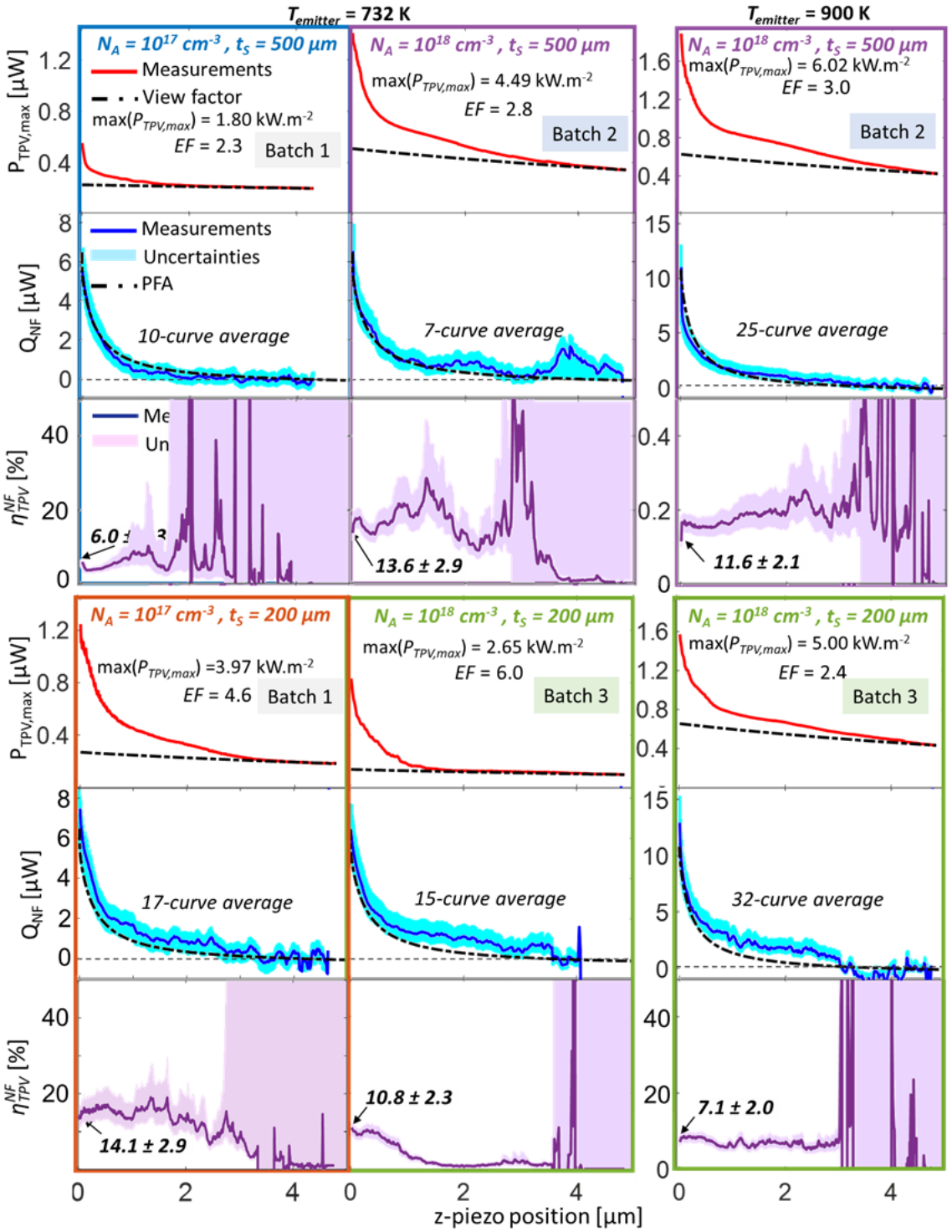

Supplementary Figure 13. Generated electrical power, near-field radiative heat flux and near-field conversion efficiency as a function of distance between a graphite emitter at 732 or 900 K and InSb TPV cells at 77 K, having an active area diameter of 20 µm, for different substrate thicknesses and p-doping levels.

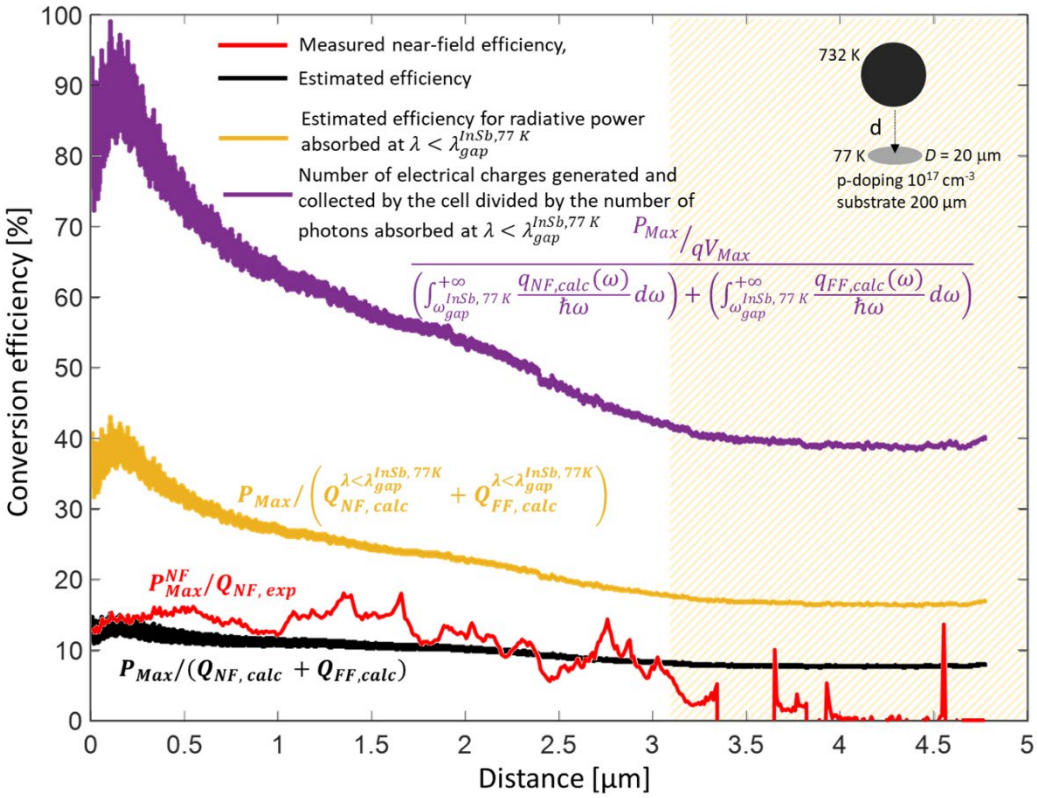

Supplementary Figure 14. Conversion efficiencies as a function of distance, respectively the near-field one in red, the total one in black, the total one for energies above bandgap in yellow, and the ratio of collected electron-hole pairs to incident photons above bandgap in purple. The 732 K graphite emitter has a diameter of 37.5 µm and the InSb TPV cell at 77 K has an active area diameter of 20 µm and a substrate thickness of 200 µm with a p-doping level of 10^{17} cm^{-3}. The thickness of the curves representing estimated efficiencies corresponds to the uncertainty depending on the relative difference between the measured $Q_{NF,exp}$ and calculated near-field radiative power $Q_{NF,calc}$. The hatched area corresponds to the distance range where there are large uncertainties on the determination of the experimental near-field conversion efficiency.

13. Power balance analysis of the experimental setup

A power balance analysis of the experimental setup (considering the power input, heat losses towards the surroundings, and an estimation of the power requested to keep the photovoltaic cell at 77 K) is performed.

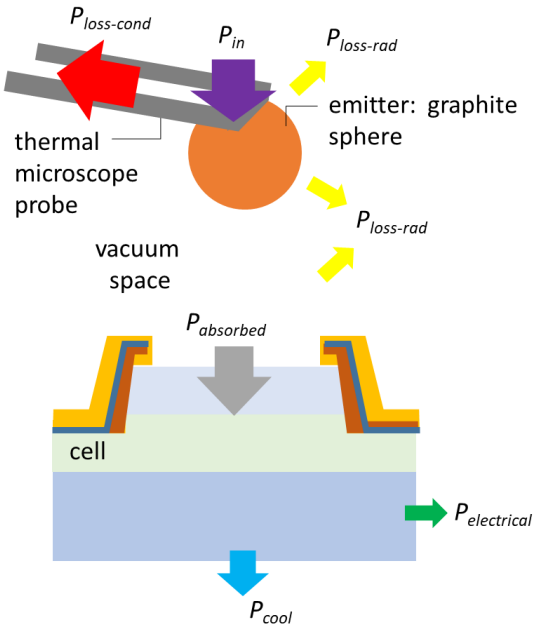

Supplementary Figure 15. Power balance analysis of the system. Even though this work focuses on the cell efficiency (PCE), a global efficiency can be estimated.

The cell efficiency (power conversion efficiency, PCE) measured in this work is defined as the ratio of the electrical power ($P_{electrical}$) to the radiative power absorbed by the cell ($P_{absorbed}$). The global conversion efficiency (GCE) is the ratio of the electrical power ($P_{electrical}$) to the power (P_{in}) supplied by Joule heating to heat up the spherical emitter. Note that the energy provided to heat the emitter is usually not accounted for in energy-harvesting applications, where the presence of a hot thermostat is considered as independent of the harvester. However, for other purposes such as spectroscopy (see conclusions of the main article), including the emitter efficiency in the analysis could be useful.
Emitter: It is well known that in contact-mode SThM, only a very-limited part of the heat input is useful for thermal conductance measurements (less than 0.5% for some of the probes): most of the heat generated by Joule effect is lost by heat conduction through the legs of the cantilever[12]. The GCE should reflect this feature. In our configuration with the sphere, thermal radiation is lost from the sphere towards environment in addition.
Cell cooling: The power required to keep the cell at 77 K (cooling system) is simply given by $P_{cool} = P_{absorbed} - P_{electrical}$. The power not absorbed by the cell corresponds to the net thermal losses (spherical thermal radiation emitter + SThM probe + cell) towards the surroundings (by thermal radiation, and conduction in the SThM probe: $P_{losses} = P_{loss\text{-}rad} + P_{loss\text{-}cond} = P_{in} - P_{absorbed}$). Note that the cell is attached to some carrier and connected to a holder with an extremity at room temperature, which conducts heat inside the vacuum chamber. The cooling power required to balance this parasitic loss is not counted here.

The Supplementary Table 1 below provides calculations of these different quantities in the case where the measured near-field PCE is 14% (see line 9 of the Supplementary Table 2 for details).

Measured near-field PCE (%)	Estimated total PCE (%)	P_{in} (µW)	$P_{electrical}$ (µW)	GCE (%)	$P_{absorbed}$ (µW)	P_{cool} (µW)	P_{losses} (µW)
14	12.4	13876.6	1.25	0.009	10.1	8.85	13866.5

Supplementary Table 1. Results of the power balance analysis for a selected case.

Results of this analysis clearly illustrate that the purpose of the work *was not to develop a full device for use in a real thermophotovoltaic conversion system* (TRL > 5), but to make a proof-of-concept in lab conditions of the near-field effects on TPV conversion (TRL = 3) with an experimental determination of the cell efficiency (PCE).

14. Summary of the results

Supplementary Table 2 sums up the main results obtained for each configuration, using either the superposition principle (*i.e* "Sup. pr.") or full measurements by scanning the whole voltage range (*i.e* "≠ V."). The best enhancement factor of 5.9 and electrical power density of 7.5 $kW.m^{-2}$ (0.75 $W.cm^{-2}$) were obtained with the sample having the largest p-doping concentration.

It must be reminded that the thermal conductance measurements require averaging over many curves. At room temperature, this is straightforward and about 100 curves allow obtaining a satisfying signal-to-noise ratio in a decent time (few hours). At low temperature, the permanent cooling of the cold finger, which does not reach quickly the stationary regime in regions far from the sample, induces a displacement, in particular laterally, of the sample that requires manual realignment of the sphere in front of the cell. This means that the time to perform experiments is much longer. As a result, averaging was performed on a smaller number of data than when done at room temperature and the near-field thermal conductance appears noisier. The long acquisition time is also the reason why the near-field efficiency was not always determined in the experiments reported in Supplementary Table 2. It must also be noted that the estimation of the far-field contribution has some influence on the determination of the near-field efficiency, which can lead to some uncertainty. As a consequence, the near-field efficiencies provided in Supplementary Table 2 should be considered with an uncertainty of ~20 %.

Method	$T_{emitter}$ [K]	p doping level [cm^{-3}]	Substrate thickness [µm]	ΔT [K]	$D_{active\ area}$ [µm]	Max TPV power [µW]	Max TPV Power density [$kW.m^{-2}$]	Max NF-TPV power [µW]	Max NF-TPV power density [$kW.m^{-2}$]	Max NF radiative flux [µW]	Estimated FF radiative flux [µW]	Estimated FF radiative power density [$kW.m^{-2}$]	Estimated total efficiency [%] (uncertainty see text)	Determined NF efficiency [%] (uncertainty see text)	NF-TPV enhancement factor
≠ V	732	10^{17}	500	655	80	2.96	0.60	0.40	0.08	-	16.8	3.34		-	1.2
≠ V	732	10^{17}	500	655	20	0.55	1.80	0.31	0.99	5.3	3.39	10.8	6.3	5.9	2.3
Sup. pr.	732	10^{17}	500	655	20	0.55	1.80	0.32	1.02	5.3	3.39	10.8	6.3	6.0	2.4
Sup. pr.	830	10^{17}	500	753	20	1.08	3.40	0.70	2.24	8.8	6.12	19.5	7.2	7.9	2.8
Sup. pr.	732	10^{17}	500	655	160	4.82	0.24	1.11	0.06	-	22.2	1.10		-	1.3
≠ V	732	10^{17}	500	655	160	5.45	0.27	0.99	0.05	7.6	22.2	1.10	18.3	13.0	1.2
Sup. pr.	732	10^{17}	200	655	20	1.28	4.10	1.05	3.20	6.5	3.20	10.2	13.2	16.2	5.6
Sup. pr.	900	10^{17}	200	823	20	1.90	6.05	1.41	4.49	14.1	7.84	25.0	8.7	10.0	4.0
≠ V	732	10^{17}	200	655	20	1.25	3.97	0.97	3.10	6.9	3.20	10.2	12.4	14.1	4.6
Sup. pr.	732	10^{18}	500	655	20	2.35	7.48	1.96	6.25	-	3.44	10.9		-	5.9
≠ V	732	10^{18}	500	655	20	2.36	7.50	1.79	5.70		3.44	10.9			4.1

Supplementary Table 2. Results of the near-field thermophotovoltaic experiments for different configurations.

Supplementary References

[1] M. Spieser, C. Rawlings, E. Lörtscher, U. Duerig, and A.W. Knoll, J. Appl. Phys. **121**, (2017).

[2] C. Luchesi, Design and development of a near-field thermophotovoltaic conversion device, PhD thesis, INSA Lyon, 2020. http://theses.insa-lyon.fr/publication/2020LYSEI053/these.pdf

[3] R. Vaillon, J.-P. Pérez, C. Lucchesi, D. Cakiroglu, P.-O. Chapuis, T. Taliercio, and E. Tournié, Opt. Express **27**, A11 (2019).

[4] D. Cakiroglu, J.P. Perez, A. Evirgen, C. Lucchesi, P.O. Chapuis, T. Taliercio, E. Tournié, and R. Vaillon, Sol. Energy Mater. Sol. Cells **203**, 110190 (2019).

[5] D. Polder and M. Van Hove, Phys. Rev. B (1971).

[6] B. V. Derjaguin, I.I. Abrikosova, and E.M. Lifschitz, Q. Rev. Chem. Soc. **10**, 295 (1956).

[7] A. Feingold and K.G. Gupta, J. Heat Transfer **92**, 69 (1970).

[8] A. Karalis and J.D. Joannopoulos, Sci. Rep. **7**, 14046 (2017).

[9] A. Datas and R. Vaillon, Nano Energy **61**, 10 (2019).

[10] N.G. Tarr and D.L. Pulfrey, IEEE Trans. Electron Devices **27**, 771 (1980).

[11] E. Blandre, P.-O. Chapuis, and R. Vaillon, Sci. Rep. **7**, (2017).

[12] S. Gomès, A. Assy, and P.-O. Chapuis, Phys. Status Solidi **212**, 477 (2015).

Corresponding author

Correspondence to Rodolphe Vaillon (rodolphe.vaillon@ies.univ-montp2.fr).